

Effect of conducting polymer incorporated heterostructure morphology of MgCo_2O_4 @PPy nanosheets: A promising cathode material for asymmetric supercapacitor applications

S Sathishkumar (✉ sathish.slm86@gmail.com)

Mahendra Institute of Engineering and Technology

M. Karthik

Mahendra Engineering College (Autonomous)

R. Boopathiraja

Chikkaiah Naicker College

M. Parthibavarman

Chikkaiah Naicker College

S. Nirmaladevi

Kongu Engineering College

S. Sathishkumar

Kongu Engineering College

Research Article

Keywords: Conducting polymer, MgCo_2O_4 , Heterostructure, Asymmetric supercapacitor, long cyclability

Posted Date: January 24th, 2022

DOI: <https://doi.org/10.21203/rs.3.rs-1276547/v1>

License: © ⓘ This work is licensed under a Creative Commons Attribution 4.0 International License.

[Read Full License](#)

Abstract

In this work, $\text{MgCo}_2\text{O}_4@\text{PPy}$ composite material was synthesized by using hydrothermal and chemical polymerization methods. In 2 M KOH electrolyte solution, the pure and composite electrodes deliver specific capacitance of 632 Fg^{-1} and 988 Fg^{-1} at a low current density of 1 Ag^{-1} . The $\text{MgCo}_2\text{O}_4@\text{PPy}$ composite electrode demonstrates high specific capacitance, long-cyclic ability, high capacitive retention, and a large energy density when utilised as an asymmetric device (ASC). A good combination of conducting polymers, which significantly improves the electrochemically active site of the electrolyte electrode interface, is credited with the $\text{MgCo}_2\text{O}_4@\text{PPy}$ composite electrode material's good electrochemical behaviour. At the same time, the heterostructure shape (Nanosheet@nanospherical) influences electrolyte solution penetration and electron/ion transport. These materials have a promising future in the realm of electrochemical energy storage.

1. Introduction

New energy and energy storage device development is becoming increasingly vital as environmental pollution and energy demand rise [1–3]. As novel energy storage systems, researchers are looking into fuel cells, Li-ion batteries, and electrochemical capacitors [4–7]. The new energy storage technology is usually environmentally benign, reusable, and efficient in converting energy [8–10]. Electrochemical capacitors (also known as supercapacitors) are becoming increasingly used all over the world. Supercapacitors are utilised in a variety of applications, including electric vehicles, computer memory storage systems, intermittent power supplies, and audio systems [11–13]. The majority of the high energy storage device is made up of electrodes and electrolytes. Supercapacitor development requires extensive materials research [14–16].

In the last few years, the unique crystal structure of spinel-structure oxides has sparked interest in the study. The spinel-type oxides' organised microstructure gives stable electrochemical performance X. The ternary oxide AB_2O_4 has been extensively studied as a high efficient anode material for supercapacitors [17, 18]. The electrode materials for reaction pseudocapacitance were found to be Te transition metal oxides. There are many charge transfer transitions in this transition metal [19]. The ligand-to-metal charge-transport transitions are common in metal oxides with high oxidation transitions [20–22]. These materials, which include the AB_2O_4 spinel with two transition metal components, usually have outstanding electrochemical performance. Cobaltite is a ternary oxide made up of cobalt and oxygen, as well as positively charged monovalent and divalent elements or groups [23]. The formula for these ternary oxides is $[\text{Am}]^z+[\text{CoxO}_y]^z$, where A is commonly an alkali metal (Na-Cs), $[\text{NH}_4]$, or Tl. The A-Co-O ternary system has diverse structural chemistry due to the flexible coordination of cobalt atoms in the system. It can be created with a variety of structures from a variety of precursors [24]. The synthesis of cobaltite and the research of its properties have sparked a lot of attention recently. Better electrode materials for supercapacitors are cobalt-based oxides with an AB_2O_4 spinel structure, such as NiCo_2O_4 [25], ZnCo_2O_4 [26], and CuCo_2O_4 [27]. MgCo_2O_4 , which has a higher theoretical capacitance (3122 F g^{-1})

than the other MCo_2O_4 TTMOs electrode components for pseudocapacitors, is a potential contender and has demonstrated great performance as electrode material in Supercapacitors [28, 29]. In recently, Zhiqiang Liu et al developed a MgCo_2O_4 -based Asymmetric device that delivers a huge energy density of 62.33 Whkg^{-1} and a power density of 750 W kg^{-1} [30].

Polypyrrole (PPy) is a flexible, environmentally stable, and electroactive conductive polymer with a high doping state conductivity ($10\text{-}100 \text{ Scm}^{-1}$). According to previous studies, wrapping PPy enhances the strong conductivity, high stability, and good electrocatalysis of metal oxides [31- 32]. Furthermore, as compared to other conductive polymers, PPy is less hazardous and easier to make. Recently Haiwen Gao et al developed an Urchin-like $\text{MgCo}_2\text{O}_4\text{@PPy}$ asymmetric supercapacitor that delivers large volumetric energy ($17.18 \text{ mWh cm}^{-3}$ at 0.16 W cm^{-3}) and outstanding cycling stability (91% of retention after 10,000 cycles) [33].

In this work, we developed $\text{MgCo}_2\text{O}_4\text{@PPy}$ electrode materials synthesized by using the hydrothermal method. The dopant p-toluenesulfonic acid can partially etch the MgCo_2O_4 heterostructure during the polymerization procedure, and the dissociative Mn/Co ions can function as a crosslinker to form a 2D PPy nanostructure. The electrochemical performance of the manufactured $\text{MgCo}_2\text{O}_4\text{@PPy}$ composite electrode was superior to that of bare MgCo_2O_4 . Furthermore, a constructed ASC based on $\text{MgCo}_2\text{O}_4\text{@PPy} // \text{AC}$ showed a high energy and power density. These impressive electrochemical displays convincingly demonstrated that the produced $\text{MgCo}_2\text{O}_4\text{@PPy} // \text{AC}$ electrode has the potential to be used in high-performance SCs.

2. Experimental Procedure

2.1. Chemicals:

All of the compounds were analytically pure and did not require any additional purification. Cobalt nitrate ($\text{Co}(\text{NO}_3)_2 \cdot 6\text{H}_2\text{O}$), magnesium nitrate ($\text{Mg}(\text{NO}_3)_2 \cdot 6\text{H}_2\text{O}$), and urea ($\text{CO}(\text{NH}_2)_2$) were all supplied by Sigma-Aldrich. Pyrrole Monomer, sodium p-Toluenesulfonate (p-TSS, $\text{C}_7\text{H}_7\text{SO}_3\text{Na}$), and ammonium persulfate ($(\text{NH}_4)_2\text{S}_2\text{O}_8$) were all acquired from India by Merck company.

2.2. Synthesis of MgCo_2O_4 nanosheets:

$\text{Mg}(\text{NO}_3)_2 \cdot 6\text{H}_2\text{O}$ (1 mmol), 2 mmol of ($\text{Co}(\text{NO}_3)_2 \cdot 6\text{H}_2\text{O}$) materials were dispersed in 50 mL D.I water and stirred continuously for 30 minutes. After the process, 4 mmol of urea was utilised as the reaction's fuel agent. Then, the homogenous solution was transferred into 50 ml Teflon lined autoclave for the hydrothermal process of 180°C for 12 hrs. After the reaction, the black product was washed many times with ethanol and D.I water to remove slags. The slag-free product was dried for 8 hours at 60°C . The product was then annealed for 3 hours at 400°C for air.

2.3. Synthesis of heterostructure MgCo₂O₄@PPy Nanosheet and nonspherical

The MgCo₂O₄@PPy heterostructure was created using the following steps:

Step (i) 1mmol of C₇H₇SO₃Na) and 20ml of D.I/ethanol Stir the solution for a few minutes to ensure uniform mixing. After that, 2 mmol of pyrrole monomer was dispersed to the aforesaid homogeneous solution (Solution A).

Step (ii) 4mmol of ammonium persulfate (NH₄)₂S₂O₈ dissolved in 30ml D.I water and stirred for a few seconds (Solution B).

Step (iii) the bundle of Nanosheet MgCo₂O₄ product was taken in a clean and pure 100ml beaker. Solution A was then added to the case, one drop at a time. After a few minutes, add solution B to the continuous polymerization process at 0- 6° C for 3-5 hours in a dark environment.

Step (IV) the polymerization product was then cleaned with ethanol and D. I water for removing certain slags, the slag free heterostructure MgCo₂O₄@PPy was dried overnight at 60° C for a hot air oven. Finally, we built at Nanosheet and Nanspherrical coated MgCo₂O₄ @PPy nanomaterial. In Fig. 1 shows the schematic representation of the MgCo₂O₄ and MgCo₂O₄/@PPy nanomaterials synthesis procedure.

2.4. Instrumentation analysis

The crystallographic structure of prepared materials was analysed by using the XRD technique (Bruker model CuK radiation ($\lambda = 1.5406$)). The surface morphology of prepared materials was analysed by using the FESM instrument (JEOL version JSM6390LV). The presenting of elements in prepared materials were identical to using the EDAX technique (JEOL version JED-2300). The surface area and pore size distribution of prepared materials were analyzed by using BET and BJH techniques (Nova 2200e model). Electrochemical behaviours of prepared samples were analysed by using a Bio-logic sp-350 and Swagelok cylindrical type instrument (TMAX-type cell).

2.5. Electrode fabrication

To carry could choose between three and two electrode systems from Bio-logic electrochemical workstation. In a three-electrode setup, Ag/AgCl serves as the reference electrode, while platinum serves as the counter electrode. The working electrodes were MgCo₂O₄ and MgCo₂O₄@PPy. In a 2M KOH electrolyte solution, the potential window was 0.0 V to 0.5 V, with diverse sweep rates ranging from 5 mVs⁻¹ to 100 mVs⁻¹ and varying current densities ranging from 1 Ag 1 to 5 Ag 1. Two electrode systems were employed to analyse the Swagelok cylindrical type instrument (TMAX-type cell): cathode as MgCo₂O₄@PPy and Anode as activated carbon with 2M PVA/KOH electrolyte solution.

3. Results And Discussion

3.1. X-ray results

In Fig. 2 shows XRD results of pure polypyrrole, MgCo_2O_4 and $\text{MgCo}_2\text{O}_4@\text{PPy}$ composite materials. The aforementioned samples have no extra feature peaks, indicating that they are very pure. There are seven prominent diffraction peaks in the XRD patterns of material at $2\theta = 31.03^\circ, 36.81^\circ, 38.27^\circ, 44.60^\circ, 55.19^\circ, 58.89^\circ,$ and 64.98° , respectively, which correspond to crystalline planes of (220), (311), (222), (400), (422), (511), and (440) according to MgCo_2O_4 (JCPDS NO. 02-1073). Other than MgCo_2O_4 , no other diffraction peak is identified, demonstrating the product's excellent purity. For MgCo_2O_4 and $\text{MgCo}_2\text{O}_4@\text{PPy}$ materials, the Scherer equation [34] was used to derive average grain sizes of 25.3 and 17.2 nm, respectively.

3.2. Morphology analysis of MgCo_2O_4 and $\text{MgCo}_2\text{O}_4@\text{PPy}$

FESEM, TEM and SAED results of MgCo_2O_4 and $\text{MgCo}_2\text{O}_4@\text{PPy}$ composite materials are shown in Fig. 3. With various magnifications, the FESEM result of bare MgCo_2O_4 nanomaterials exhibits a bundle of nanosheet like morphology (Fig. 3a, b). FESEM pictures of $\text{MgCo}_2\text{O}_4@\text{PPy}$ composite material are shown in Fig. 3 (c, d). The $\text{MgCo}_2\text{O}_4@\text{PPy}$ composite material has heterostructure morphology similar to that of a surface coated (Nano-spherical) nanosheet. The nanosheets were surface coated on nanospherical after the polymerization process. The heterostructure is a structure that is utilised to improve the electrochemical behaviour of the ion transport process. The EDAX result of $\text{MgCo}_2\text{O}_4@\text{PPy}$ composite material is shown in Fig. 3 (e), which confirms the identity of Mg, Co, O, and N without any impurities. TEM pictures of MgCo_2O_4 and $\text{MgCo}_2\text{O}_4@\text{PPy}$ composite materials with various magnifications are shown in Fig. 3 (f-h). The nanosheet and spherical-like morphology are visible in the TEM images. The SAED pattern of $\text{MgCo}_2\text{O}_4@\text{PPy}$ composite materials is shown in Fig. 3 (i).

3.3. N_2 adsorption and desorption

The surface area and pore size distribution were determined using Burner-Emmett-Teller (BET) and Barrett-Joyner-Halenda (BJH) analyses. The surface area and pore sized distribution of MgCo_2O_4 and $\text{MgCo}_2\text{O}_4@\text{PPy}$ materials are shown in Fig. 4 (a). Based on IUPAC classifications, the plot clearly shows that both electrodes are mesoporous, as indicated by the Type IV isotherm with H3 hysteresis loop. This loop's observed P/P_0 ranges from 0.6 to 1.0. The bare MgCo_2O_4 electrode has a BET surface area of $76 \text{ m}^2/\text{g}$, whereas the $\text{MgCo}_2\text{O}_4@\text{PPy}$ electrode has a massive surface area of $103 \text{ m}^2/\text{g}$. The BJH method was used to analyse the pore size values. The pore diameters of pure and composite electrode materials are 20 nm and 9 nm, respectively. Electrodes with a tiny pore size and the most surface area will perform better electrochemically. The porous and broad surface structure supplied a large number of ions or electrons, an excellent interacting electrolyte contact, and a fast faradaic redox reaction [35]. In the MgCo_2O_4 electrode sample, the polypyrrole (PPy) coated MgCo_2O_4 ($\text{MgCo}_2\text{O}_4@\text{PPy}$) electrode has a higher surface area than the MgCo_2O_4 electrode. This is owing to the interconnected nonspherical structure of PPy, which has more nanogap and nanopores. After covering PPy, the 1D spherical reveals

the FESEM picture. The hybrid heterostructure (Nanosheets interconnect with nano spherical) provided extensive active sites for the adsorption and desorption processes, as well as ion-electron travel, resulting in good capacitive performance.

3.4. XPS analysis

XPS was used to analyse the oxidation states of elements and chemical compositions of the heterostructure of MgCo₂O₄@PPy nanocomposite shown in Fig. 4 (b-f). The survey spectrum of MgCo₂O₄@PPy nanocomposites contains Mg, Co, O, and N, as shown in Fig. 4 (b). In Fig. 4 (c) shows the XPS spectrum of Mg 1s and Mg 2p. The XPS spectrum of Mg 1s, which exhibits a peak with a binding energy of 1304.5 eV, further proves Mg's existence. The presence of magnesium oxide is indicated by the peak at a binding energy of 51.1 eV in the XPS spectra of Mg 2p [36]. The magnified spectrum of Co 2p_{1/2} and Co 2p_{3/2} was clearly shown in Fig. 4 (d). Figure 4 (d) exhibits the Co 2p spectrum, which depicts the two forms of Co 2p. Peaks with combined energies of 781.1 and 796.7 eV should correspond to Co 2p_{3/2} and Co 2p_{1/2} [37], respectively. In Fig. 4 (e), the binding energies for the three oxygen contributions in the O1s spectrum, O1, O2, and O3, are 529.5, 531.8, and 532.4 eV, respectively. O1 and O2 are represented by metal oxygen binding (M-O-M), another specie O3, is a hydroxide specie, which means it has chemically or physically absorbed water on its surface [38]. Figure 4 (f) shows polypyrrole with a single N1s peak at 399.0 eV, indicating a pyrrolic N relation [39].

3.5 Application studies (Electrochemical)

3.5.1 Analysis of Cyclic voltammetry (CV)

Figure 5 (a-c) illustrates the electrochemical cyclic voltammetry data of pure polypyrrole, MgCo₂O₄ and MgCo₂O₄@PPy composite electrodes. The cyclic voltammetry analysis of pure polypyrrole, MgCo₂O₄, and MgCo₂O₄@PPy composite electrodes were examined by using 2 M KOH electrolyte solution at various sweep speeds ranging from 5 to 100 mVs⁻¹. The CV curves of the three electrodes show large and visible redox peaks, demonstrating the material's pseudocapacitive properties. From CV, the specific capacitance values of pure polypyrrole, MgCo₂O₄, and MgCo₂O₄@PPy electrodes are 202, 412, and 534 Fg⁻¹, respectively. The CV investigation involved several sweep rate currents at various diffusion-controlled (faradaic) and surface controlled (capacitive) conduct charge storage systems. A power law [40] governs the relationship between log i_p and log v for both behaviours.

$$i_p = a' V^b \text{ ————— (1)}$$

The charge collected on the surface controls redox processes in electrolyte ions, which explains a statement of Log I proportional log v. The composite electrode b value of anodic and cathodic peaks positioned at 0.45 and 0.57 indicates a semi-infinite diffusive regulated mechanism for faradaic behaviour. The R-S equation [41] describes the link between peak current and sweep rate in a Trasatti technique equation-based diffusion-controlled process. The total capacitance of the MgCo₂O₄@PPy composite electrode is shown in Fig. 5 (g). The total capacitance of the MgCo₂O₄@PPy electrode was

examined using the square root of scan rates vs $1/\text{capacitance}$. The plot shows the total capacitance values of 909 Fg^{-1} . Figure 5 (h) illustrates the capacitive contribution of the $\text{MgCo}_2\text{O}_4@\text{PPy}$ electrode displayed as $1/\text{square root of scan rate vs capacitance}$ at various scan rates ranging from 5 to 100 mVs^{-1} . In Fig. 5 (i) shows the capacitive contribution of $\text{MgCo}_2\text{O}_4@\text{PPy}$ electrode exhibits 5.7%, 6%, 8%, 9.4%, 10.8%, 11.9% and 13.8% of 5, 10, 20, 40, 60, 80, and 100 mVs^{-1} respectively.

3.5.2 Analysis of galvanostatic charge-discharge (GCD)

Figure 6 (a-c) displays the GCD results of pure PPy, MgCo_2O_4 , and $\text{MgCo}_2\text{O}_4@\text{PPy}$ composite electrodes with different current densities of 1 Ag^{-1} to 5 Ag^{-1} . The GCD profile clearly shows non-linear curves, which could be related to the electrodes' pseudocapacitive nature. The specific capacitance values of pure PPy, MgCo_2O_4 , and $\text{MgCo}_2\text{O}_4@\text{PPy}$ composite electrodes are 137, 692, and 988 Fg^{-1} , respectively, at a low current density of 1 Ag^{-1} , as shown in Fig. 6. (d-f). The capacitance retention of MgCo_2O_4 and $\text{MgCo}_2\text{O}_4@\text{PPy}$ electrode materials after 10,000 cycles is shown in Fig. 6 (g, h). After 10,000 cycles, the capacitive retention of pure MgCo_2O_4 and $\text{MgCo}_2\text{O}_4@\text{PPy}$ electrodes is 79% and 93%, respectively.

3.5.3 Analysis of electrochemical impedance spectroscopy (EIS)

Supercapacitor development has depended heavily on impedance spectroscopy measurements. In most impedance data, Z' and Z'' represent the real and imaginary components, respectively. The EIS of pure PPy, MgCo_2O_4 , and $\text{MgCo}_2\text{O}_4@\text{PPy}$ composite electrode materials is shown in Fig. 6 (i). The intersection of the curve at real part Z' represents the internal resistance (R_s), which is the total of the electrolyte's ionic resistance, active materials' intrinsic resistance, and contact resistance at the active material-collector interface. The PPy, MgCo_2O_4 , and $\text{MgCo}_2\text{O}_4@\text{PPy}$ composite electrodes had internal resistances of 0.3, 3.4, and 6.5Ω , respectively. The semicircle of the $\text{MgCo}_2\text{O}_4@\text{PPy}$ electrode has a substantially smaller diameter than the semicircle of the MgCo_2O_4 and PPy electrode, indicating that the ppy coating improved charge transfer over bare materials. The PPy, MgCo_2O_4 , and $\text{MgCo}_2\text{O}_4@\text{PPy}$ composite electrodes had charge transfer resistances of 19, 17, and 13Ω , respectively.

3.5.4 Fabrication of $\text{MgCo}_2\text{O}_4@\text{PPy}//\text{AC}$ based asymmetric supercapacitor (ASC) applications

The asymmetric supercapacitor of the $\text{MgCo}_2\text{O}_4@\text{PPy}//\text{AC}$ device was built using the Swagelok instrument. The cell was assembled by Cathode material as $\text{MgCo}_2\text{O}_4@\text{PPy}$ and anode materials like activated carbon with gel type 2 M KOH/PVA electrolyte solution. The comparison CV results of the $\text{MgCo}_2\text{O}_4@\text{PPy}$ electrode and the activated carbon electrode are shown in Fig. 7 (a). Figure 7 (b, c) depicts the CV and GCD result of an asymmetric device with various scan speeds ranging from 5 to 100 mVs^{-1} and current density ranging from 1 Ag^{-1} to 5 Ag^{-1} . Fig. 7 (d) shows the specific capacitance values of ASC device delivers 98 Fg^{-1} at a current density of 1 Ag^{-1} . The b value of the ASC device anodic and cathodic values of 0.5 to 0.8 ranges reveal semi-in restricted diffusive behaviour for pseudo-

capacitive nature, as shown in image 7 (e). Fig. 7 (f, g) illustrates the total capacitance and capacitive contribution of the ASC device. For ASC devices, the capacitive contribution ratio for various sweep rate values is 15%, 20%, 27%, 37%, 60%, 63% and 83% for various sweep rates. This ASC device's cyclic stability is 84% after 10,000 cycles with a high current density of 5 Ag^{-1} . The schematic representation of the $\text{MgCo}_2\text{O}_4\text{@PPy//AC}$ charge storage mechanism is shown in Fig. 8 (a). When compared to the Ragone plot of the newest MgCo_2O_4 -based ASC device results in Fig. 8(b), the manufactured ASC device provides a high energy density of 40 Whkg^{-1} and a massive power density of 1544 Whkg^{-1} at a low current of 1 Ag^{-1} . These are exceptionally high values when compared with the other MgCo_2O_4 based ASC devices, such as MgCo_2O_4 Nanosheet//AC (12.99 Whkg^{-1} ; 448.9 Whkg^{-1}) [42], MgCo_2O_4 THSs//AC (30.6 Whkg^{-1} ; 861 Whkg^{-1}) [43], $\text{MgCo}_2\text{O}_4\text{@PPy//AC}$ (33.4 Whkg^{-1} ; 320 Whkg^{-1}) [44], $\text{MgCo}_2\text{O}_4\text{@NiMoO}_4\text{//AC}$ (37.5 Whkg^{-1} ; 480 Whkg^{-1}) [45], MgCo_2O_4 SMPs//AC (39.7 Whkg^{-1} ; 396 Whkg^{-1}) [46].

Conclusion

In this work, the bundle of MgCo_2O_4 nanosheets and heterostructure of $\text{MgCo}_2\text{O}_4\text{@PPy}$ materials were synthesized by using hydrothermal and chemical polymerization methods. The prepared materials were analysed by using XRD, FESM, TEM with SAED, XPS and BET surface analyzer. The XRD results confirm the presents of the MgCo_2O_4 phase without any other materials. The morphology result of the pure MgCo_2O_4 sample exhibits a bundle of nanosheets like morphology and composite material exhibits heterostructure morphology of nanospherical coated nanosheet like morphology. In this heterostructure, morphology improves electrochemical behaviour. XPS data confirm the oxidation state and chemical composition of the $\text{MgCo}_2\text{O}_4\text{@PPy}$ material. The BET and BJH results show that the $\text{MgCo}_2\text{O}_4\text{@PPy}$ material has a high surface area of $103 \text{ m}^2/\text{g}$ and the smallest pore size of 9 nm in the mesoporous region, implying that they may easily interact with the electrolyte, which is important for obtaining outstanding electrochemical performance. The electrochemical behaviours were analysed by using three and two electrode systems. In a three-electrode system, the $\text{MgCo}_2\text{O}_4\text{@PPy}$ electrode delivers high specific capacitance of 988 Fg^{-1} at low current 1 Ag^{-1} compared with pure electrode materials of PPy, MgCo_2O_4 respectively. The $\text{MgCo}_2\text{O}_4\text{@PPy //AC}$ ASC cell has a high specific capacitance of 98 Fg^{-1} at 1 Ag^{-1} and an 84% capacitive retention after 10,000 cycles. The $\text{MgCo}_2\text{O}_4\text{@PPy //AC}$ ASC cell has a massive energy density of 40 Whkg^{-1} and a power density of 1544 Wkg^{-1} when fully built. Overall, the $\text{MgCo}_2\text{O}_4\text{@PPy}$ electrode demonstrates to be an effective electrode material for supercapacitor use.

References

1. J.R. Miller, P. Simon, Electrochemical capacitors for energy management. Science Magazine **321**(5889), 651–652 (2008)
2. B. Pandit, B.R. Sankapal, P.M. Koinkar, Novel chemical route for $\text{CeO}_2\text{/MWCNTs}$ composite towards highly bendable solid-state supercapacitor device. Sci. Rep **9**, 5892 (2019)

3. M.R. Lukatskaya, O. Mashtalir, C.E. Ren, Y. Dall'Agnese, P. Rozier, P.L. Taberna, M. Naguib, P. Simon, M.W. Barsoum, Y. Gogotsi, Cation intercalation and high volumetric capacitance of two-dimensional titanium carbide. *Sci* **341**(6153), 1502–1505 (2013)
4. H. Shi, S. Chen, W. Shi, Z. Peng, J. Li, Z. Liu, G. Zhang, L. Liu, High performance fibre-shaped supercapacitors based on core-shell fibre electrodes with adjustable surface wrinkles and robust interfaces. *Mater. Chem. A* **9**(31), 16852–16859 (2021)
5. K. Yousefipour, R. Sarraf-Mamoory, A. Yourdkhani, Supercapacitive properties of Nickel Molybdate/rGO Hybrids prepared by the hydrothermal method. *Surf. Interfaces*, (2021) 101638
6. M. Shoeb, M. Mobin, S.M. Adnan, I.I. Ansari, M.N. Khan, S. Zaidi, M.Y. Ansari, *Facile Synthesis of a Gr-Ag/PIn Nanocomposite as a Binder Free Electrode for High-Performance Supercapacitor Application* (*Surf. Interfaces*, 2021), p. 101650
7. M. Shang, C. Xing, W. Ding, C. Huang, Construction of asymmetric flexible-solid state supercapacitors based on Mo-MnO₂ nanoflowers and MoO_{3-x} nanobelts. *Surf. Interfaces* **27**, 101502 (2021)
8. M. Khairy, S.A. El-Safty, Hemoproteins–nickel foam hybrids as effective supercapacitors. *Chem. Commun.* **50**(11), 1356–1358 (2014)
9. S. Ishaq, M. Moussa, F. Kanwal, M. Ehsan, M. Saleem, T.N. Van, D. Losic, Facile synthesis of ternary graphene nanocomposites with doped metal oxide and conductive polymers as electrode materials for high performance supercapacitors. *Sci. Rep.* **9**(1), 1–11 (2019)
10. B. Guo, X. Wang, P.F. Fulvio, M. Chi, S.M. Mahurin, X.G. Sun, S. Dai, Soft-templated mesoporous carbon-carbon nanotube composites for high performance lithium-ion batteries. *Adv. Mater* **23**(40), 4661–4666 (2011)
11. X. Yue, R. Hu, D. Zhu, J. Qi, Y. He, Q. Meng, F. Wei, Y. Ren, Y. Sui, Controlled synthesis and formation mechanism of flower-like CuS/NiS microspheres for supercapacitors. *Surf. Interfaces* **22**, 100871 (2021)
12. D. Prakash, S. Manivannan, N. B co-doped and Crumpled Graphene Oxide Pseudocapacitive Electrode for High Energy Supercapacitor. *Surf. Interfaces* **23**, 101025 (2021)
13. A. UmaSudharshini, M. Bououdina, M. Venkateshwarlu, C. Manoharan, P. Dhamodharan, Low temperature solvothermal synthesis of pristine Co₃O₄ nanoparticles as potential supercapacitor. *Surf. Interfaces* **19**, 100535 (2020)
14. S. Zhu, L. Li, J. Liu, H. Wang, T. Wang, Y. Zhang, L. Zhang, R.S. Ruoff, F. Dong, Structural directed growth of ultrathin parallel birnessite on β -MnO₂ for high-performance asymmetric supercapacitors. *ACS Nano* **12**(2), 1033–1042 (2018)
15. S. Zhu, T. Wang, X. Liu, Y. Zhang, F. Li, F. Dong, H. Zhang, L. Zhang, Low-charge-carrier-scattering three-dimensional α -MnO₂/ β -MnO₂ networks for ultra-high-rate asymmetrical supercapacitors. *Appl. Energy Mater* **2**(2), 1051–1059 (2018)
16. C. Jiang, W. Ding, H. Wu, Z. Yu, L. Ma, Z. Zou, Hierarchical Li₄Ti₅O₁₂ nanosheet arrays anchoring on carbon fibre cloth as ultra-stable free-standing anode of Li-ion battery. *Ceram. Int.* **44**(3), 3040–3047

(2018)

17. R. BoopathiRaja, M. Parthibavarman, The cost-effective asymmetric supercapacitor from binary MnCo_2O_4 electrodes with nanofiber and nanocube-like morphology. *J. Mater. Sci.: Mater. Electron*, **31**(13) 2020
18. R. BoopathiRaja, M. Parthibavarman, A.N. Begum, Hydrothermal induced novel $\text{Cu Co}_2\text{O}_4$ electrode for high performance supercapacitor applications. *Vacuum* **165**, 96–104 (2019)
19. V. Vignesh, K. Subramani, M. Sathish, R. Navamathavan, Electrochemical investigation of manganese ferrites prepared via a facile synthesis route for supercapacitor applications. *Colloid. Surface. A* **538**, 668–677 (2018)
20. X. Wu, L. Meng, Q. Wang, W. Zhang, Y. Wang, A high performance asymmetric supercapacitor based on carbon fibre coated with MgCo_2O_4 nanobrush. *Mater. Lett.* **206**, 71–74 (2017)
21. S. Gu, Z. Lou, X. Ma, G. Shen, CuCo_2O_4 nanowires grown on a Ni wire for high-performance, Flexible fibre supercapacitors. *Chem. Electro. Chem.* **2**, 1042–1047 (2015)
22. J. Xu, Y. Sun, M. Lu, L. Wang, J. Zhang, J. Qian, X. Liu, Fabrication of hierarchical $\text{MnMoO}_4 \cdot \text{H}_2\text{O} @ \text{MnO}_2$ core-shell nanosheet arrays on nickel foam as an advanced electrode for asymmetric supercapacitors. *Chem. Eng, J.* **334**, 1466–1476 (2018)
23. L. Manjakkal, A. Pullanchiyodan, N. Yogeswaran, E.S. Hosseini, R. Dahiya, A Wearable Supercapacitor Based on Conductive PEDOT: PSS-Coated Cloth and a Sweat Electrolyte. *Adv. Mater.* **32**, 1907254 (2020)
24. X.L. Guo, J.M. Zhang, W.N. Xu, C.G. Hu, L. Sun, Y.X. Zhang, Growth of NiMn LDH nanosheet arrays on KCu_7S_4 microwires for hybrid supercapacitors with enhanced electrochemical performance. *J. Mater. Chem. A* **5**, 20579–20587 (2017)
25. R. BoopathiRaja, M. Parthibavarman, Reagent induced formation of NiCo_2O_4 with different morphologies with large surface area for high performance asymmetric supercapacitors. *Chem. Phys. Let* **755**, 137809 (2020)
26. H. Yu, H. Zhao, Y. Wu, B. Chen, J. Sun, Electrospun $\text{ZnCo}_2\text{O}_4/\text{C}$ composite nanofibers with superior electrochemical performance for supercapacitor. *J. Phys. Chem. Solids* **140**, 109385 (2020)
27. J. Sun, C. Xu, H. Chen, A review on the synthesis of CuCo_2O_4 -based electrode materials and their applications in supercapacitors. *J. Mater* **7**(1), 98–126 (2021)
28. S.G. Krishnan, M.V. Reddy, M. Harilal, B. Vidyadharan, I.I. Misnon, M.H. Ab Rahim, J. Ismail, R. Jose, Characterization of MgCo_2O_4 as an electrode for high performance supercapacitors. *Electrochim. Act* **161**, 312–321 (2015)
29. L. Cui, L. Huang, M. Ji, Y. Wang, H. Shi, Y. Zuo, S. Kang, High-performance MgCo_2O_4 nanocone arrays grown on three-dimensional nickel foams: preparation and application as binder-free electrode for pseudo-supercapacitor. *J. Power Sources* **333**, 118–124 (2016)

30. Z. Liu, A. Li, Y. Qiu, Q. Zhao, Y. Zhong, L. Cui, W. Yang, J.M. Razal, C.J. Barrow, J. Liu, MgCo₂O₄@NiMn layered double hydroxide core-shell nanocomposites on nickel foam as superior electrode for all-solid-state asymmetric supercapacitors. *J. Colloid Interface Sci.* **592**, 455–467 (2021)
31. J. Hu, M. Li, F. Lv, M. Yang, P. Tao, Y. Tang, H. Liu, Z. Lu, Heterogeneous NiCo₂O₄@ polypyrrole core/sheath nanowire arrays on Ni foam for high performance supercapacitors. *J. Power Sources* **294**, 120–127 (2015)
32. J. Zhao, J. Wu, B. Li, W. Du, Q. Huang, M. Zheng, H. Xue, H. Pang, Facile synthesis of polypyrrole nanowires for high-performance supercapacitor electrode materials. *Prog. Nat. Sci.* **26**(3), 237–242 (2016)
33. H. Gao, X. Wang, G. Wang, C. Hao, S. Zhou, C. Huang, An urchin-like MgCo₂O₄@ PPy core-shell composite grown on Ni foam for a high-performance all-solid-state asymmetric supercapacitor. *Nanoscale* **10**(21), 10190–10202 (2018)
34. V. Shanmugavalli, K. Vishista, Low-cost synthesis of cubic spinel structured high efficient NiCo₂O₄/polyaniline nanocomposite for supercapacitor application. *Mater. Res. Express* **6**(4), 045021 (2019)
35. A.K. Mondal, D. Su, S. Cehen, A. Ung, H. Kim, G. Wang, Mesoporous MnCo₂O₄ with a flake-like structure as advanced electrode materials for lithium-ion batteries and supercapacitors, *Chem. Eur J.* **20**, 1–8 (2014)
36. Z. Huang, Z. Wang, X. Zheng, H. Guo, X. Li, Q. Jing, Z. Yang, Effect of Mg doping on the structural and electrochemical performance of LiNi_{0.6}Co_{0.2}Mn_{0.2}O₂ cathode materials. *Electrochim. Acta* **182**, 795–802 (2015)
37. H. Chen, G. Jiang, W. Yu, D. Liu, Y. Liu, L. Li, Q. Huang, Electrospun carbon nanofiberic coated with ambutan-like NiCo₂O₄ microspheres as electrode materials. *Mars. Commun.* **7**, 90–96 (2017)
38. P. Wu, S. Cheng, M. Yao, L. Yang, Y. Zhu, P. Liu, O. Xing, J. Zhou, M. Wang, H. Luo, M. Liu, A low-cost, self-standing NiCo₂O₄@ CNT/CNT multilayer electrode for flexible asymmetric solid-state supercapacitors. *Adv. Funct. Mater.* **27**(34), 1702160 (2017)
39. J. Shao, X. Li, L. Zhang, Q. Qu, H. Zheng, Core-shell sulfur@polypyrrole composites as high capacity materials for aqueous rechargeable batteries. *Nanoscale* **5**, 1460 (2013)
40. J. Wang, J. Polleux, J. Lim, B. Dunn, Pseudocapacitive contributions to electrochemical energy storage in TiO₂ (Anatase). *J. Phy. Chem* **111**(40), 14925–14931 (2017)
41. K.V. Sankar, R.K. Selvan, D. Meyrick, Electrochemical performance of CoFe₂O₄ nanoparticles and an rGO based asymmetric supercapacitor, *Rsc. Adv.* **5**, 99959 (2015)
42. S. Vijayakumar, S. Nagamuthu, K.-S. Ryu, In situ preparation of MgCo₂O₄ nanosheets on Ni-foam as a binder-free electrode for high performance hybrid supercapacitors. *Dalton Trans.* **47**, 6722–6728 (2018)
43. Y. Wang, X. Ma, S. Li, J. Sun, Y. Zhang, H. Chen, C. Xu, Facile solvothermal synthesis of novel MgCo₂O₄ twinned-hemispheres for high performance asymmetric supercapacitors. *J. Alloys Compd.*

818, 152905 (2020)

44. H. Gao, X. Wang, G. Wang, C. Hao, S. Zhou, C. Huang, An urchin-like $\text{MgCo}_2\text{O}_4@ \text{PPy}$ core-shell composite grown on Ni foam for a high-performance all-solid-state asymmetric supercapacitor. *Nanoscale* **10**(21), 10190–10202 (2018)
45. H. Gao, X. Wang, G. Wang, C. Hao, C. Huang, C. Jiang, Facile construction of a $\text{MgCo}_2\text{O}_4@ \text{NiMoO}_4/\text{NF}$ core-shell nanocomposite for high-performance asymmetric supercapacitors. *J. Mater. Chem. C* **7**(42), 13267–13278 (2019)
46. H. Gao, Y. Li, H. Zhao, J. Xiang, Y. Cao, A general fabrication approach on spinel MCo_2O_4 (M= Co, Mn, Fe, Mg and Zn) submicron prisms as advanced positive materials for supercapacitor. *Electrochim. Acta* **262**, 241–251 (2018)

Figures

Figure 1

shows a schematic representation of the $\text{MgCo}_2\text{O}_4@ \text{PPy}$ synthesis procedure.

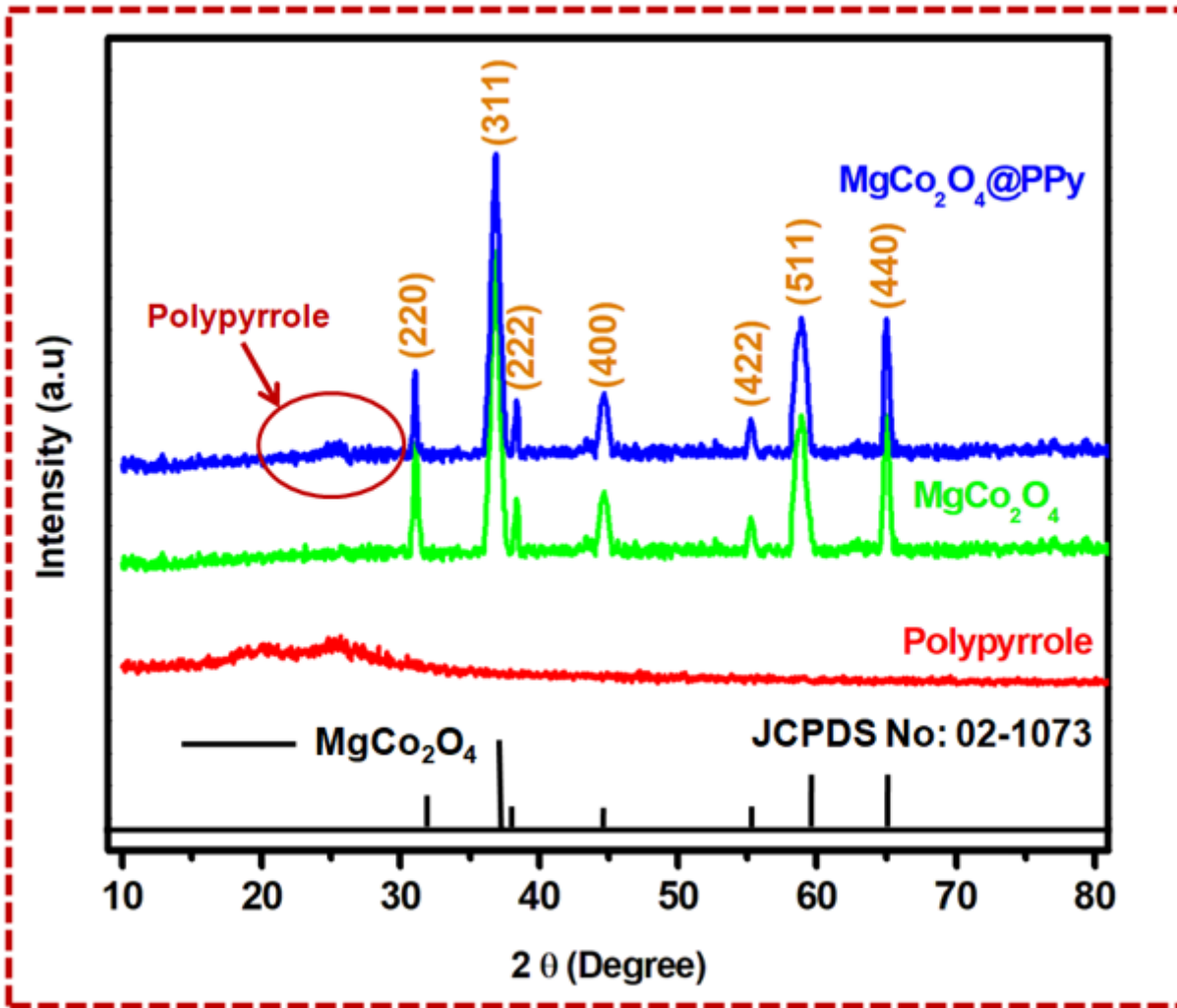


Figure 2

shows the XRD result of pure polypyrrole, MgCo₂O₄ and MgCo₂O₄@PPy composite material

Figure 3

shows FESEM and TEM with SAED results of MgCo₂O₄ and MgCo₂O₄@PPy materials. (a, b) shows FESEM images of pure MgCo₂O₄ material; (c, d) shows the FESEM image of MgCo₂O₄@PPy composite material; (e) shows EDAX result of MgCo₂O₄@PPy composite material; (f-h) shows TEM images of pure MgCo₂O₄ and MgCo₂O₄@PPy composite material. (i) Depicts SAED pattern of MgCo₂O₄@PPy composite material.

Figure 4

(a) shows BET surface area and BJH pore size distribution of $MgCo_2O_4$ and $MgCo_2O_4@PPy$ materials; (b-f) shows the XPS result of $MgCo_2O_4@PPy$ composite material; (b) depicts survey spectrum of $MgCo_2O_4@PPy$; (c) XPS result of Mg 2p and Mg 1s spectrum; (d) XPS result of CO 2p; (e) XPS result of O 1s spectrum; (f) XPS result of N 1s spectrum

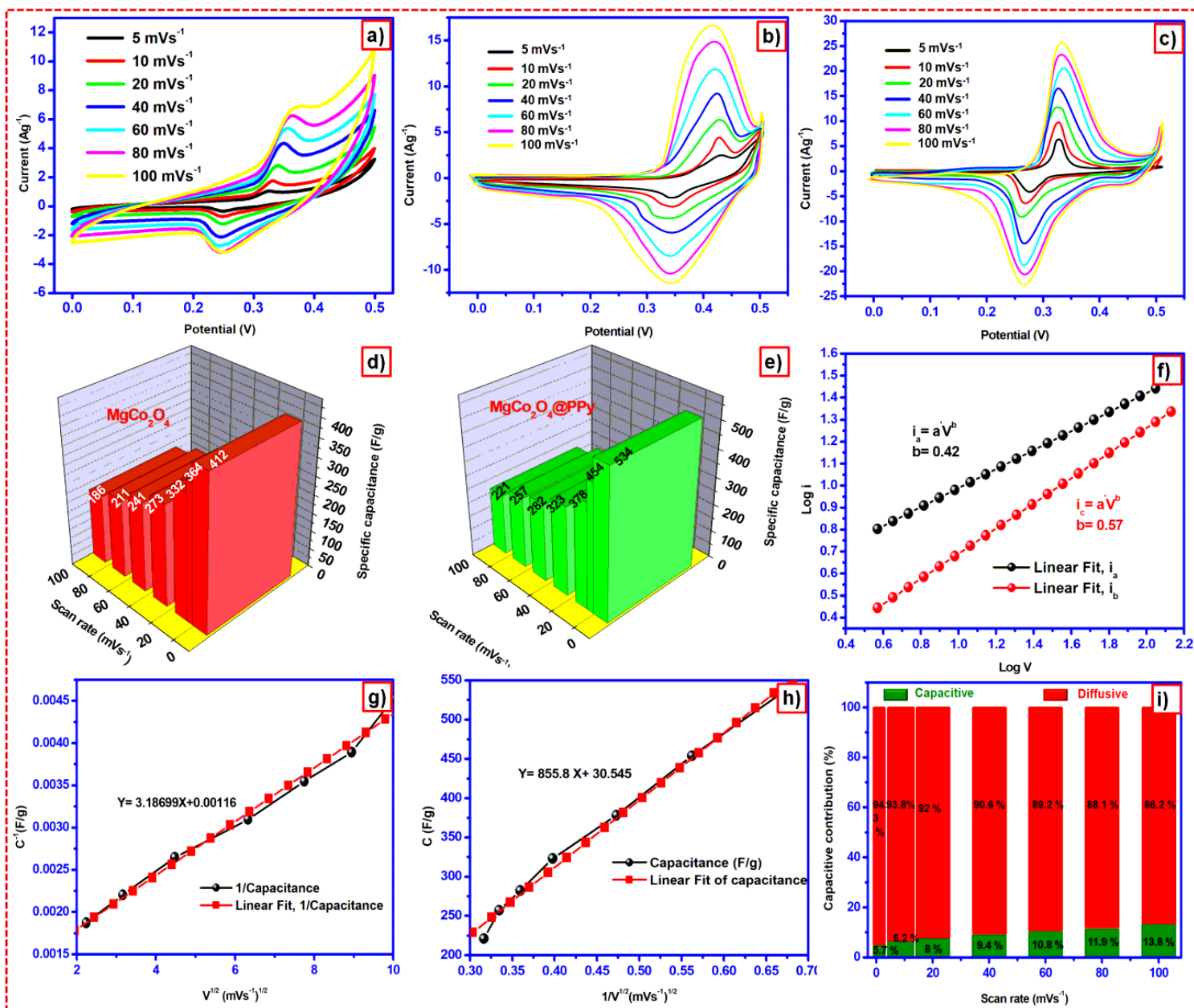


Figure 5

shows electrochemical cyclic voltammetry result of pure polypyrrole, $MgCo_2O_4$ and $MgCo_2O_4@PPy$ electrodes with different scan rates of 5 mVs^{-1} to 100 mVs^{-1} ; (a) CV result of Polypyrrole electrode; (b) CV result of bare $MgCo_2O_4$ electrode; (c) CV result of $MgCo_2O_4@PPy$ electrode; (d, e) depicts specific capacitance values of $MgCo_2O_4$ and $MgCo_2O_4@PPy$ electrodes with different scan rates 5 mVs^{-1} to 100 mVs^{-1} . (f) The plot of Log i vs Log v; (g) shows total capacitance of $MgCo_2O_4@PPy$ electrode plotted by

the square root of scan rate vs 1/capacitance; (h) capacitive contribution of MgCo₂O₄@PPy electrode plotted by 1/ square root of scan rate vs capacitance; (i) Shows the capacitive contribution (EDLC and Pseudo) parts of MgCo₂O₄@PPy electrodes.

Figure 6

shows Galvanostatic charge/discharge result of pure polypyrrole, MgCo₂O₄, and MgCo₂O₄@PPy electrodes with different current densities of 1 Ag⁻¹ to 5 Ag⁻¹; (a) GCD result Pure Polypyrrole electrode; (b) GCD result of bare MgCo₂O₄ electrode; (c) GCD result of MgCo₂O₄@PPy electrodes; (d-f) depicts specific capacitance values of pure polypyrrole, MgCo₂O₄, and MgCo₂O₄@PPy electrodes with different current densities 1 Ag⁻¹ to 5 Ag⁻¹; (g, h) depicts capacitive retention of MgCo₂O₄, and MgCo₂O₄@PPy electrodes after 10,000 cycles; (i) Electrochemical impedance spectroscopy result in pure polypyrrole, MgCo₂O₄, and MgCo₂O₄@PPy electrodes.

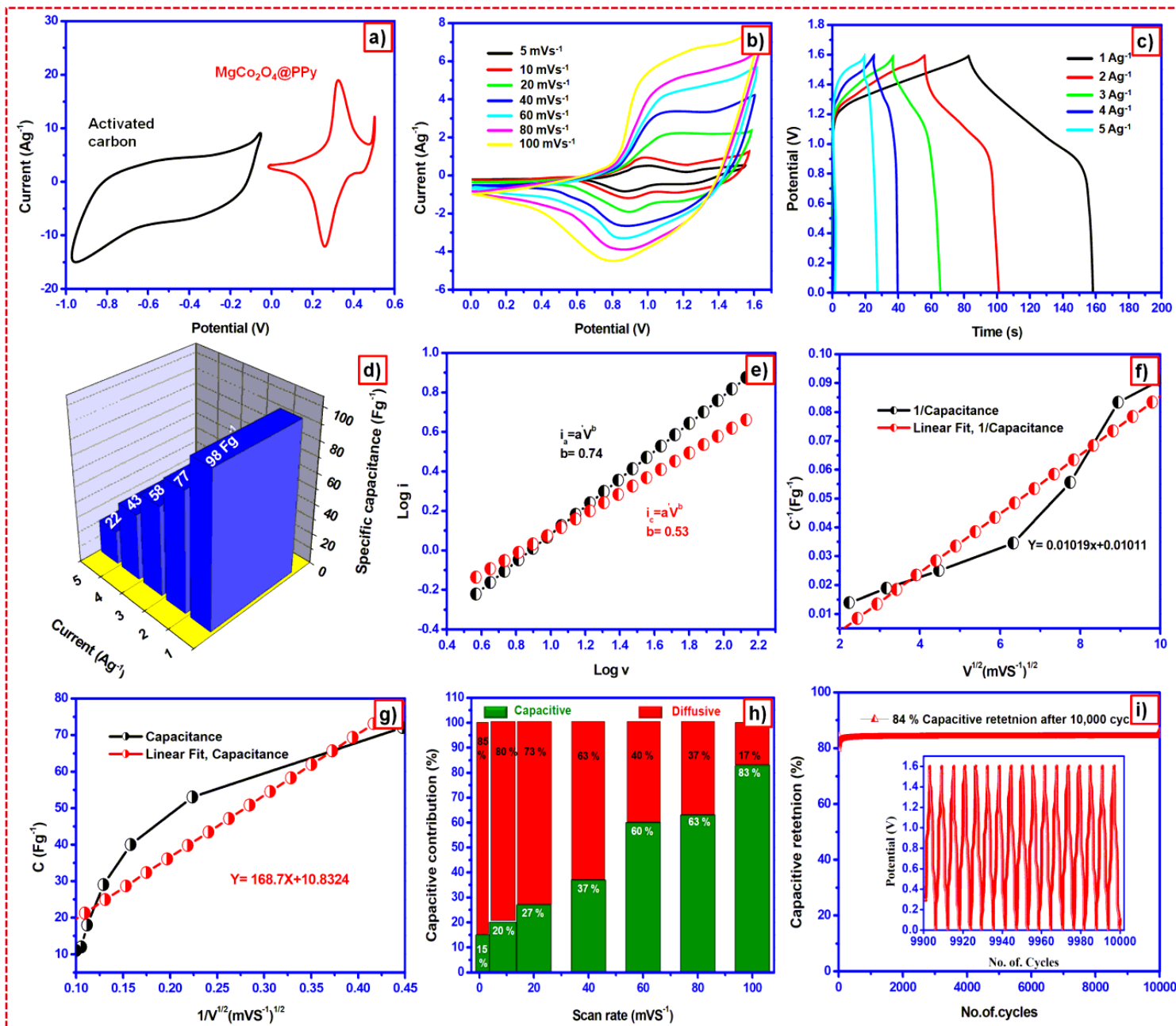


Figure 7

shows the electrochemical result of fabricated $\text{MgCo}_2\text{O}_4\text{@PPy//AC}$ asymmetric supercapacitor (ASC); (a) shows the comparison result of $\text{MgCo}_2\text{O}_4\text{@PPy}$ and Activated carbon CV result; (b) CV result of ASC cell with different scan rates 5 mVs^{-1} to 100 mVs^{-1} ; (c) GCD result of ASC cell with a different current density of 1 Ag^{-1} to 5 Ag^{-1} ; (d) depicts specific capacitance values of ASC device CV result with different current densities 1 Ag^{-1} to 5 Ag^{-1} ; (e) Plot of $\text{Log } I$ vs $\text{Log } v$; (f) shows total capacitance of ASC device plotted by the square root of scan rate vs $1/\text{capacitance}$; (g) capacitive contribution of ASC device plotted by $1/\text{square root of scan rate vs capacitance}$; (h) shows the capacitive contribution (EDLC and Pseudo) parts of ASC device; (i) depicts capacitive retention of ASC cell delivers 84 % after 10,000 cycles.

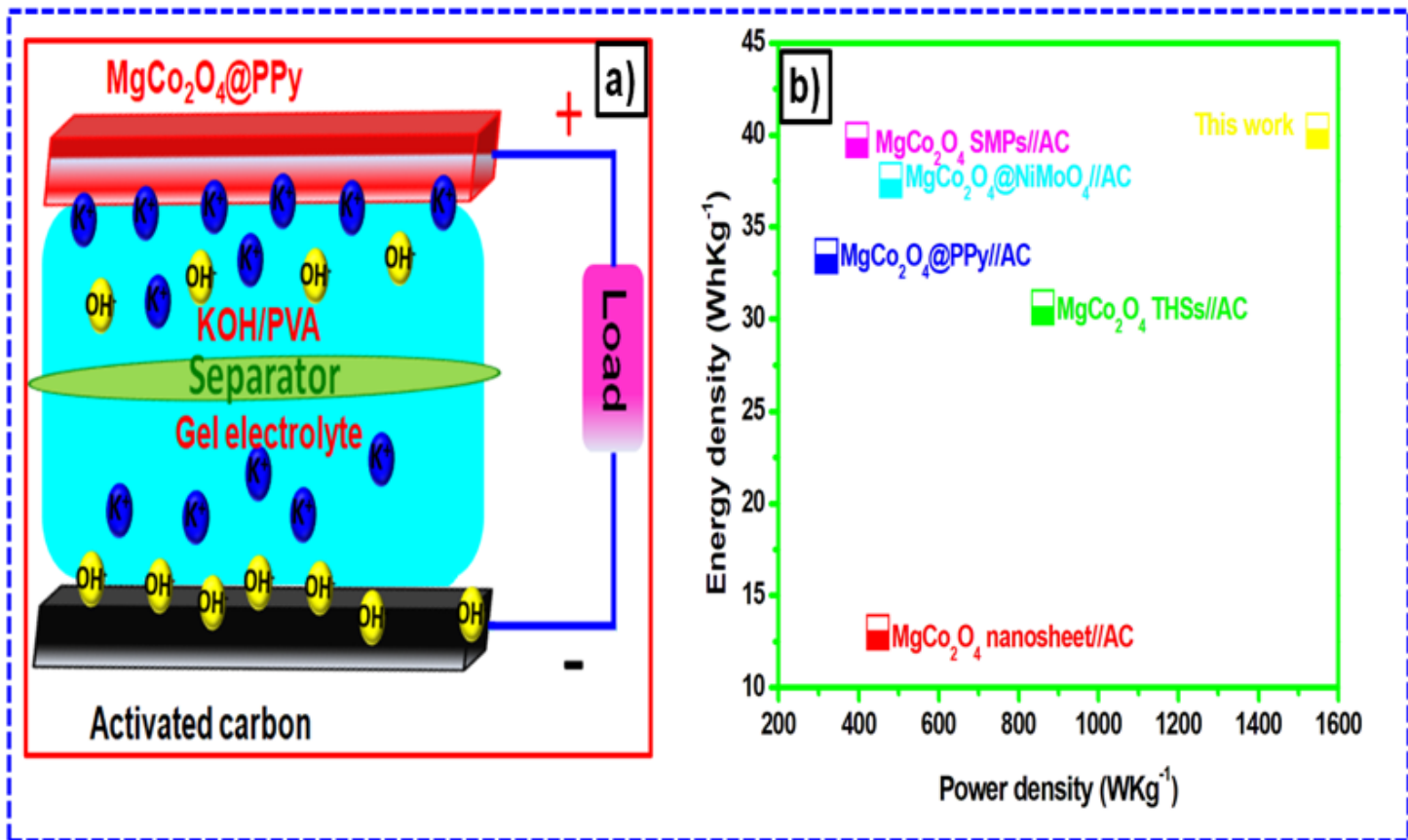


Figure 8

(a) shows a schematic representation of the ASC device charge storage mechanism; (b) shows Ragone plots related to energy and power densities in comparison with that of previously reported state-of-the-art supercapacitors.